A novel machine learning method to exploit EBSD and nanoindentation for TRIP steels microstructures analysis

Federico Bruno [a,b], Georgios Konstantopoulos [c], Gianluca Fiore [a], Edoardo Rossi [d],
Marco Sebastiani [d], Costas Charitidis [c,*], Luca Belforte [b], Mauro Palumbo [a]

[a] Department of Chemistry, University of Turin, Via Pietro Giuria 7, 10125 Torino, Italy
[b] Centro Ricerche Fiat, C.R.F. S.C.p.A., Corso Settembrini 40, 10135 Torino, Italy
[c] RNANO Lab.—Research Unit of Advanced, Composite, Nano-Materials & Nanotechnology, School of Chemical Engineering, National Technical University of Athens, GR-15773 Zographos, Athens, Greece
[d] Department of Civil, Computer Science, and Aeronautical Technologies Engineering, Roma Tre University, Via Vito Volterra 62, 00146 Rome, Italy

ABSTRACT

The recognition of phases and microstructures in TRIP-assisted bainitic-ferritic steels is challenging and requires sophisticated techniques to gain insights and reveal mechanical features with nanoscale precision. EBSD and nanoindentation have been employed to assess the surface composition and their properties within a reporting depth of 30 nm. Correlative mechanical microscopy and data science were used to overcome the shortcomings associated with the lack of an inclusive solution that combines the metadata from both techniques. A modular methodology is presented, which involves routines for exploiting structural and mechanical data via reproducible Machine Learning models (code and data are shared). The approach is structured to facilitate reuse by research community for correlating characterization mapping data, not limited to nanoindentation and EBSD. Gaussian mixture models are adopted to extract mechanical phases utilizing the nanomechanical properties. The K-means++ method is used for the first time to mine information from Inverse Polar Figure (IPF) mapping about anisotropy and to extract the knowledge from images for each grain, including grain coordinates and size. Moreover, k-nearest-neighbours regression was used to perform data imputation to fill in the values of descriptors related to missing coordinates relative to those of nanoindentation, grain boundary, EBSD phase, and EBSD anisotropy maps.

1. Introduction

Correlative microscopy is becoming increasingly important in materials science. This approach combines different microscopy and mechanical characterization techniques to study material properties, thereby exploiting the potential of each method [1].

In this study, the concept was applied to study the mechanical features at the grain level of TRIP-assisted bainitic-ferritic (TBF) steel. This material belongs to the TRIP (Transformation induced plasticity) steel family, and it has a bainitic-ferritic matrix obtained through the austempering process. In the automotive industry, these steels are valued in a lightweight design and commonly used in Body In White (BIW)

components [2]. Characterization of phases/microstructures (P/M) in TRIP steels can meet the steelmaker's and users' requirements to correlate mechanical properties with P/M, which is of great significance in component performance and can provide helpful feedback in engineering process design [3]. In this respect, nanoindentation can be an essential technique for rapidly mining statistically significant information about steels. This method had the benefit of measuring the hardness and elastic modulus of materials at the nanoscale with a minimal surface alteration, because contact area and depth are fairly smaller than traditional micromechanical testing, such as micro-hardness and bending tests.

In particular, the structure/–property relationship can be studied

upon subsequent thermal treatments by overcoming three bottlenecks. The first consists of knowing the correct position (coordinates) and size of grains and martensite laths. The second challenge is to indent a specific grain in a precise crystallographic plain. The last one is to overcome the knowledge gaps that arise from missing data in the characterization datasets.

Regarding the first problem, the interpretation of EBSD data alone is not sufficient to distinguish BCC structures of ferrite, martensite, and bainite. Conversely, austenite, which has an FCC lattice, is easy to recognize. EBSD images are usually processed in commercial software using the Hough transform to annotate the characterization data and perform phase mapping. Commonly, a down-sampling process is performed by the software, while the user selects up to three elements for phase recognition to narrow down the number of possible phases. Both steps contribute to the reduction of the information collected by EBSD [4]. Lately, commercial versions of EBSD software have been able to differentiate ferrite and martensite through a supervised machine learning approach [5], although there are many other approaches with notable advantages over the traditional Hough method. These, however, require assumptions about the structure and the phases [6]. Nonetheless, this approach cannot always be used when P/M are too fine in size. Moreover, it is impossible to differentiate bainite with these tools because it is composed of alternating ferrite and cementite lamellae (upper bainite) or cementite lamellae dispersed within ferrite needles (lower bainite). To address these challenges, different ways to exploit EBSD data, such as Band Contrast (BC), Band Slope (BS), and Kernel Average Misorientation (KAM), have been proposed [7–11].

As for the second problem, hardness and elastic modulus are affected by P/M intercepted by the nanoindenter tip. Many nanoindentation studies are complemented by EBSD analyses [7,12–15] to study anisotropy [16–18], martensitic transformation [19,20], and tip-sample contact zone. It is essential to ensure that the indent size is smaller than the average grain size, thereby minimizing the influence of other P/M on the measured mechanical properties. Another possible issue is the indentation being made on top of a grain boundary, and in this case, mechanical features will depend even more on the P/M mixture in the indentation volume of the interaction site [14,21]. Thus, these factors have increased the necessity for the development of nanoindentation protocols with depth sensing capability and high precision. Such protocols enable ultra-shallow indentations, reducing the inter-indent spacing required to improve the lateral resolution of the test [22]. Finally, advancements in high-speed (up to 1 indent per second) nanoindentation in Continuous Stiffness Measurement (CSM) mode have enabled the acquisition of large amounts of data [23]. This fact can allow the establishment of unbiased structure–property relationships for complex materials [24].

Considering the third problem of missing data, it can significantly impact scientific outcomes, given the importance of the resolution on the studied materials [25]. To address the impact of missing data on the size of the datasets and, consequently, on the prediction accuracy of machine learning models, the production of synthetic data based on real-world data has been proposed. The SMOTE (Synthetic Minority Oversampling Techniques) method is one recognized approach for this purpose [26]. Suppose the missing data is not a result of misalignment but rather due to actual gaps in measurements, then imputation techniques can be used to estimate the missing values using the available data. Common imputation methods include mean imputation, median imputation, multiple imputation, and knn imputation. Mean imputation assumes that the value of an intermediate point, positioned between two other points, is the mean value of those two data points. In contrast, k-NN imputation can demonstrate a strategic benefit, especially for example when applied on predicting missing image data. This method uses 'k' nearest neighbors, based on a metric such as Euclidean distance, to calculate the expected pixel color RGB value. This approach can be an efficient solution when combining multiple phase maps corresponding to the same region of interest. It is essential to precisely retain and

compare only the exact matches of the coordinates to obtain a validated and unbiased outcome.

Of quite importance is assuring that the nanoindentation protocol tuning enables to obtain a representative of bainitic steels response, since the individual phase responses are dimensionally related to grain size and thickness. In addition, for nanoindentation measurements, it is required to ensure that the requirements for a clean, flat, and well-polished surface are met to satisfy the standards for high-quality data generation [27,28]. In this study, the surface quality standards were met using the protocol required to prepare the surface for EBSD characterization (as reported in section 2.1). Also, a shallow depth of 30 nm was used, which enables the isolation of individual responses, while even not exhaustively studied in the literature, this depth range resulted in loads varying from 0.1 to 0.4 mN, thus mitigating pop-in effects which have a cumulative probability to occur upon the application of loads of 0.4 mN or higher depending on the surface preparation method [29]. However, it has been widely reported that pop-in phenomena might affect the recorded mechanical behavior and are essential to consider in materials science fields, ranging from conventional applications to more sophisticated such as in the study of materials used in nuclear fusion [30]. Specifically, pop-in phenomena might occur due to the phase transformation, the dislocations and ground boundaries present, and the relative size of the indenter to the size of the grain. On the other hand, the homogeneity of phases indented (single phase indentation), the high purity of the high strength bainitic trip steels studied can be essential factors to prevent the frequency of such responses since the evidenced cementite was less than 0.9 % and the indentation depth was 30 nm to satisfy that in most occasions a single phase is penetrated, whereas in case of grain boundaries indentation, this has been indicated through the algorithmic implementation. Moreover, the indent spacing can be another factor affecting the occurrence of pop-in phenomena. The employed nanoindentation protocol involved an interindent spacing which was 8.6 times larger than the maximum indentation depth, which is close to the 10-times rule conventionally employed in nanoindentation. However, considering that at shallow depth the mechanical response is not dominated plastically as in an indentation at hundred nanometer or micrometer scale, this mitigated the probability of occurrence of pop-in or pile-up. Finally, in the region of interest no pop-in phenomena related to the phase transformation of austenite are reported since austenite was not detected by EBSD characterization.

In this paper, nanoindentation and EBSD techniques were used to distinguish the phases and microstructures in a sample by overlaying the surface characterization on the same ROI (Region of Interest). The aim of correlating structural and mechanical data was to enhance the accuracy of nanoindentation mechanical phase analysis. The correlation is essential for accurately linking the mechanical properties with the P/M, where factors like phase anisotropy, grain boundaries, and grain size significantly influence the mechanical response and the detection of the unique phase characteristics. The core idea consists of correlating a structural phase map by EBSD and a mechanical phase map by nanoindentation measurements. The approach is designed to overcome the problems as mentioned earlier. For this purpose, an innovative nanoindentation protocol was tailored for phases and microstructures recognition and their nanomechanical properties determination of TBF steel (Bainitic – Ferritic TRIP steel). This protocol enables fast mapping (3 s per CSM indent) with a maximum depth of 30 nm and a dataset size of about 25,000 CSM nanoindents. To calibrate the post-processing of nanoindentation measurements, an EBSD analysis was previously carried out on the sample, combining information about anisotropy and phases/microstructures. Based on the image analysis subsequently performed by clustering, the knowledge from the extracted IPF map was mined, and the EBSD parameters/descriptors were used to identify the BCC phases (bainite, ferrite, martensite). This characterization data was further processed using Python and R language code to refine EBSD maps and identify the phases and their contours by pixel-wise classification. A consensus algorithm was then applied to classify each phase at

Table 1
TBF-1000 elemental composition.

C (at. %)	Mn (at. %)	P (at. %)	S (at. %)	Si (at. %)	Al (at. %)	Ti + Nb + V (at. %)	Cr + Mo (at. %)
0.190	2.36	0.010	0.001	0.606	0.234	0.060	0.03

the grain level. d. To the best of the authors' knowledge, this is the first time that phase mapping has been performed at grain level and with such a massive amount of nanoindentation data. In contrast, existing literature studies combining EBSD with nanoindentation typically conduct analysis on the spot (x,y) coordinate pairs or pixel-wise [31–34].

## 2. Materials and methods

2.1. Materials

A TBF-1000 steel was analysed, having the elemental composition described in Table 1 and provided by Centro Ricerche Fiat. A 3x3 cm plate was cut to perform chemical composition analysis by means of a Quantometer (ThermoScientific ARL 3460 OES) following normative ASTM E415-21 [35].

The sample was cold-mounted in conductive resin and then mechanically polished using standard sandpapers with colloidal silica 40 nm for final polishing [36].
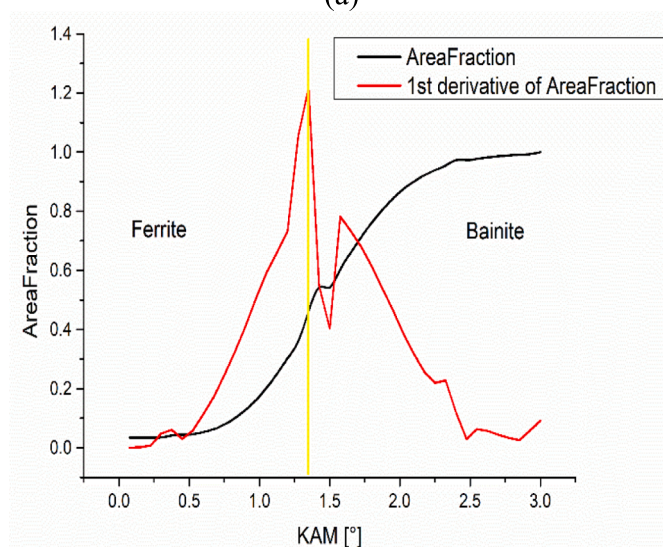
Prior to the EBSD analysis, carbon tape was placed around the sample's surface and the mounting resin. This step was taken to improve further the conductibility of mounted sample, hence EBSD (electron backscatter diffraction pattern) resolution. Finally, before performing the nanoindentation, the carbon tape was carefully removed.
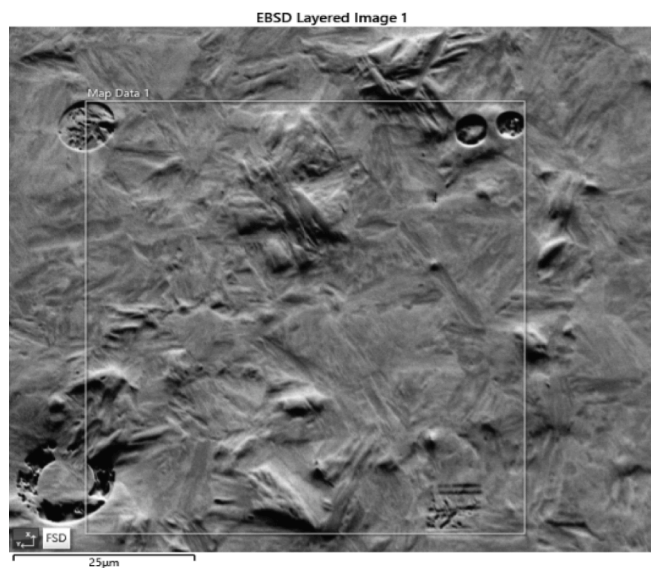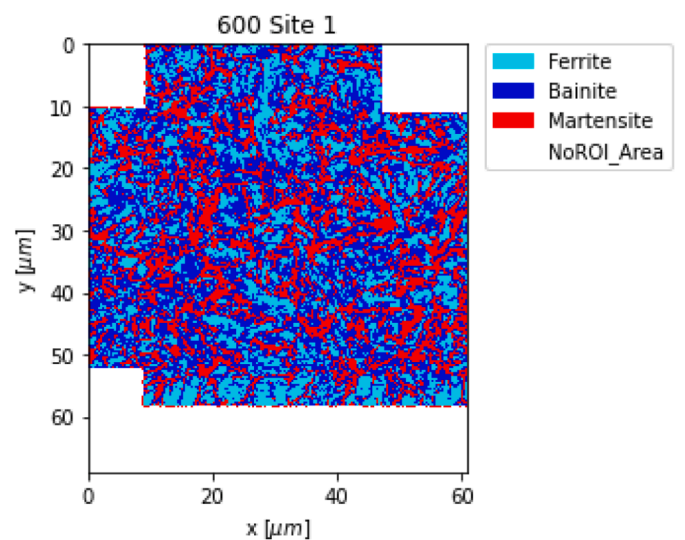

(a)
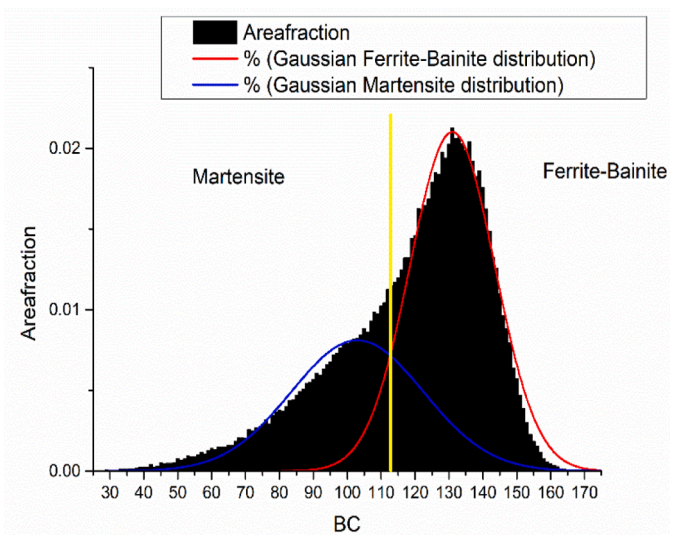
(b)

(c)

(d)

Fig. 1. (a) SEM-FSD Image of EBSD ROI area, (b) Martensite – ferrite/bainite mixture distinction using Band-Contrast values. Separation value: 113, (c) Ferrite-bainite distinction using KAM values. Separation value: 1.35°, (d) Phases and microstructure distribution. In this case austenite grains were not detected and carbides amount was negligible. Step size was equal to 0.1745 μm.
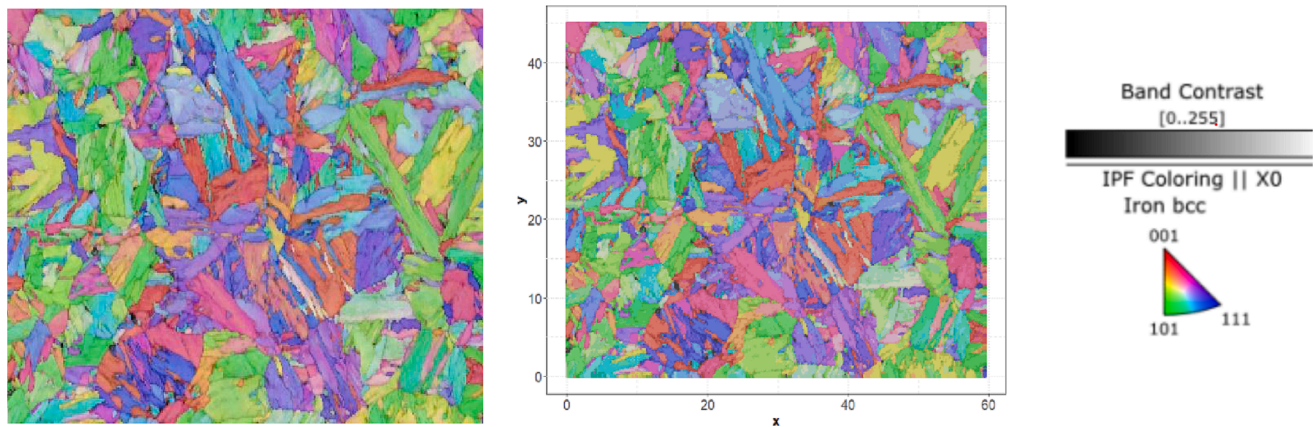
Fig. 2. IPF grain anisotropy maps across the X-axis direction; (left) original image, (middle) k-means++ clustered image with 50 color shades. The scale is reported in μm scale. (right) Memo of the IPF maps.

2.2. Methods

For SEM-EBSD analysis (SEM Tescan FESEM 9000: 20 kV; 1nA; EBSD Symmetry S2 Oxford Instruments; Data are provided by AztecCrystal). ROI area: 66.55 μm x 68.75 μm. Kernel average misorientation (KAM) was calculated using a kernel 9x9 set as maximum KAM 3° [7,9].

The CSM nanomechanical testing of the samples was performed using an FT-I04 (FemtoTools AG, Zurich, Switzerland), with noise floors down to 500 pN in force and 50 pm in displacement. A Berkovich tip with a 50 nm radius was used, which is attached to a MEMS force sensor with range from 0 to 20 mN. The Femto-Indenter enables the comprehensive study of mechanical behavior of materials with a high resolution and accuracy across depth. In both quasistatic and CSM testing, the calibration was performed on a standard fused quartz sample within the depth ranges of testing to establish a precise tip-area-function to measure the contact area during nanoindentation with high precision.

A CSM nanoindentation displacement-controlled protocol was tailored to the multiphase TBF steels studied, to provide a large-scale map of 25,000 nanoindents which high accuracy, achieving a speed of 3 sec per indent. The selected CSM frequency after tuning was 150 Hz, and the amplitude started from 0.4 nm with a 5 % amplitude ratio, respectively, and the maximum penetration depth was 35 nm. The interindent spacing was 0.3 μm and the dimensions of nanoindentation pattern were 60 μm x 45 μm. The reporting depth was selected at 30 nm in close relation with the resolution depth of EBSD, and to obtain the main contribution of each individual phase and grain boundaries. Nanomechanical properties were extracted in accordance with the Oliver-Pharr method [37].

Data analysis was carried out with Python (EBSD phases classification, thresholding to isolate grain boundaries map) and R language (refine the phase maps of EBSD and nanoindentation at grain level and perform the correlation of maps by matching each individual coordinate of the phase maps, and perform data imputation). R Studio is an open-source software and provides a coherent, flexible system for data analysis. R language was used to implement every algorithm involved in clustering and classification tasks. All computations were performed using 64-bit Windows 10 Home (Intel ® Core™ i5-8250U CPU @ 1.60 GHz, 1801Mhz 4 Cores, 8 Logical Processors and 24.00 GB RAM). The complete R code and part of data used/generated in this study are available in the GitHub. The EBSD-nanoindentation method allows to assign for each phase/microstructure the relative features. This method can be used (partially as a module, or as a whole) for all metals and alloys. This type of study has a considerable importance on an industrial level. Indeed, nanoindentation is a fast (sample preparation and measurement), cheap and precise tool for nanostructure characterization. The creation of an artificial intelligence model that can accept as input the nanoindentation raw data and provide as an output the phases and microstructures assignments provides an enormous advantage in engineering studies. The creation of an artificial intelligence model which can accept as input the nanoindentation raw data and provide as an output the phases and microstructures assignments represents an enormous advantage in engineering studies, due to the fact that it can be used to reconstruct and mine information from images in literature and other sources.

3. Results and discussion

3.1. EBSD analysis - phases and microstructures recognition

EBSD analysis was performed to study the samples' anisotropy and phases/microstructures. The outcomes of this analysis were then used to inform the nanoindentation experiments. Before the EBSD analysis, some milling marks were made using a Focused Ion Beam (FIB) microscope equipped with a Gallium source. These marks were used to delimitate the ROI area to facilitate sample orientation for both nano-indentation and EBSD maps (Fig. 1a).

To recognize phases and microstructures, a method reproduced by literature is proposed [10]. This approach utilizes Band Contrast (BC) and Kernel Average Misorientation (KAM) as descriptors to identify the threshold values for recognizing P/M and obtain pixel-level P/M labelling. The protocol is broken down into eight sequential steps:

1. Map clean up: Before data processing, it is necessary to eliminate the points close to FIB marks and correct any electronic drifts (if any). This step improves the precision of the P/M recognition process.
2. All pixels labeled as austenite and cementite are locked as EBSD can reliably recognize these structures. Only BCC phases are selected for further classification. In this study, no austenite was detected, and the amount of carbides was negligible.
3. Select all BCC labeled pixels.
4. Count the number of pixels for each value of BC and calculate the area fraction.
5. Use Gaussian curves to find the distribution of martensite and ferrite-bainite (F-B) mixture, by identifying the intercept point at the x coordinate where the Gaussian curves intersect (Fig. 1b) [10].
6. Count the amount of F-B pixel for each value of KAM and calculate area fraction.
7. Calculate the cumulative distribution of KAM values within the measurement area, using a step of 0.0075° to achieve good curve resolution (Fig. 1c) [9].
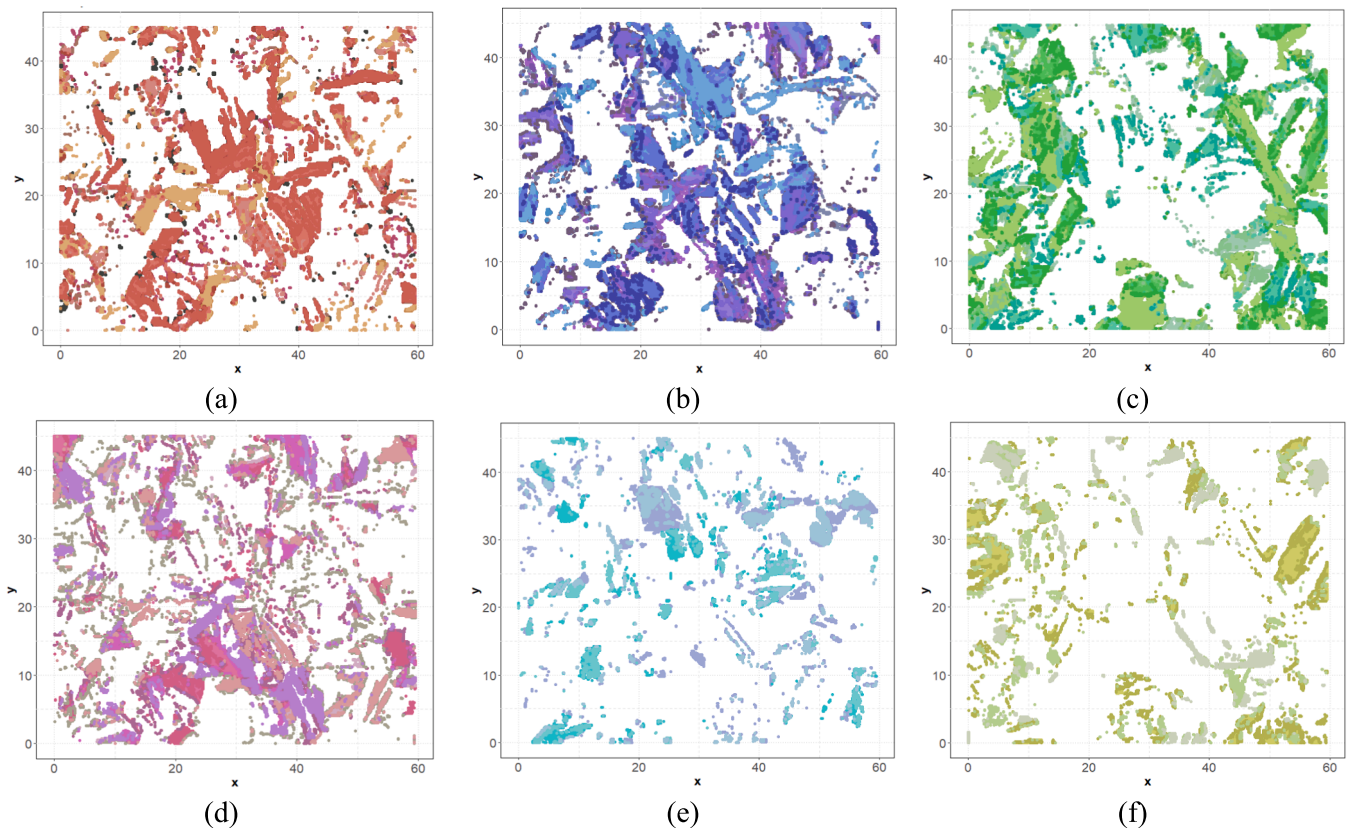8. Plot the phases/microstructures map (Fig. 1d).

Fig. 3. Crystallographic plane clustering using Euclidean distance method. Each relevant anisotropic orientation has been isolated and corresponds to: (a) (0 0 1) plane, (b) (1 1 1) plane, (c) (1 0 1) plane, (d) (0 0 1)U(1 1 1) plane, (e) (1 0 1)U(1 1 1) plane, (f) (0 0 1)U(1 0 1) plane.

The statistical fitting approach used Gaussian mixture models. This process was optimized by the Expectation-Maximization algorithm to classify the data corresponding to martensite. Following this, the rest of data were subsequently treated with the described statistical fitting procedure and optimiser. This enabled the separation of bainite data from the ferrite data using the KAM parameter.

3.2. EBSD analysis and Inverse Polar Figure maps – Grain properties detection (anisotropy, size, location)

Inverse Polar Figures (IPF) were used to study the orientation of crystallographic planes in the samples (See Fig. 2 left). In the IPF image, each individual grain is characterized by two distinct features: a unique color and its boundaries, which are indicated by the x and y coordinates. This information is essential for researchers conducting EBSD analysis, especially for subsequent phase extraction based on EBSD mapping parameters. This step is often overlooked in a significant number of investigations [38,39], where it's expected that each grain should correspond to only one phase. IPF maps are handy to study anisotropy within a sample.

Thus, the first step in the analysis was to perform image clustering on the IPF image. The number of clusters needed was chosen to ensure that the same level of detail in the map is retained. This clustering was performed using the k-means algorithm. This is an efficient strategy to treat colors since the original image contained several thousands of color shades. By applying the k-means algorithm, the color shades were reduced to 50, yet retaining the same level of information (See Fig. 2 right).

EBSD commercial software does not enable exporting a data frame containing information about crystallographic planes from IPF raw data; labels of the planes are missing, while only data referring to the step of the measurement for each 250 nm by x- and y-axis is reported rather

than providing the information for each pixel. More specifically, the software generates a dataset with the colors in RGB values (Red, Green, Blue) indicating the anisotropy. To interpret this data, an algorithm was developed which takes the color shades from the k-means clustered image as input. The colors Euclidean distance was used to compare the 50 color shades with the 6 main colors of a memo in order to annotate the crystallographic planes. The selection of only 6 colors in the memo was based on the available crystallographic planes, (0 0 1), (1 0 1), and (1 1 1), as well as their combinations, which is meaningful. Additionally, the white color was included to represent the mixture of all colors (and planes), and the black color was used to indicate the lack of signal in the specific location rather than to denote the grain boundaries.

The results illustrated in Fig. 3 were used as a basis for the subsequent steps of the methodology, which aims to identify the coordinates of each grain. After clustering the color values, the k-means++ method was applied to cluster the x and y coordinates. This approach was chosen because, in addition to color, the coordinates are the second feature distinguishing grains in IPF maps. The process led to creating over 3000 clusters, corresponding to the six crystallographic planes. The goal was to allocate as many clusters as possible, following a data-driven grouping of values. This approach helped determine the necessary number of clusters in an organic manner. On the contrary, k-means++ would not allocate any data to clusters that were not necessary or naturally occurring. In addition, a filter was added to automatically remove any clusters with fewer than five datapoint observations. In Fig. 4 some indicative grains are presented, showcasing the efficiency of grain detection with the proposed methodology.

3.3. Grain boundaries segmentation

The following step involved leveraging the IPF crystallographic plane map, its band contrast, and the transition between the individual
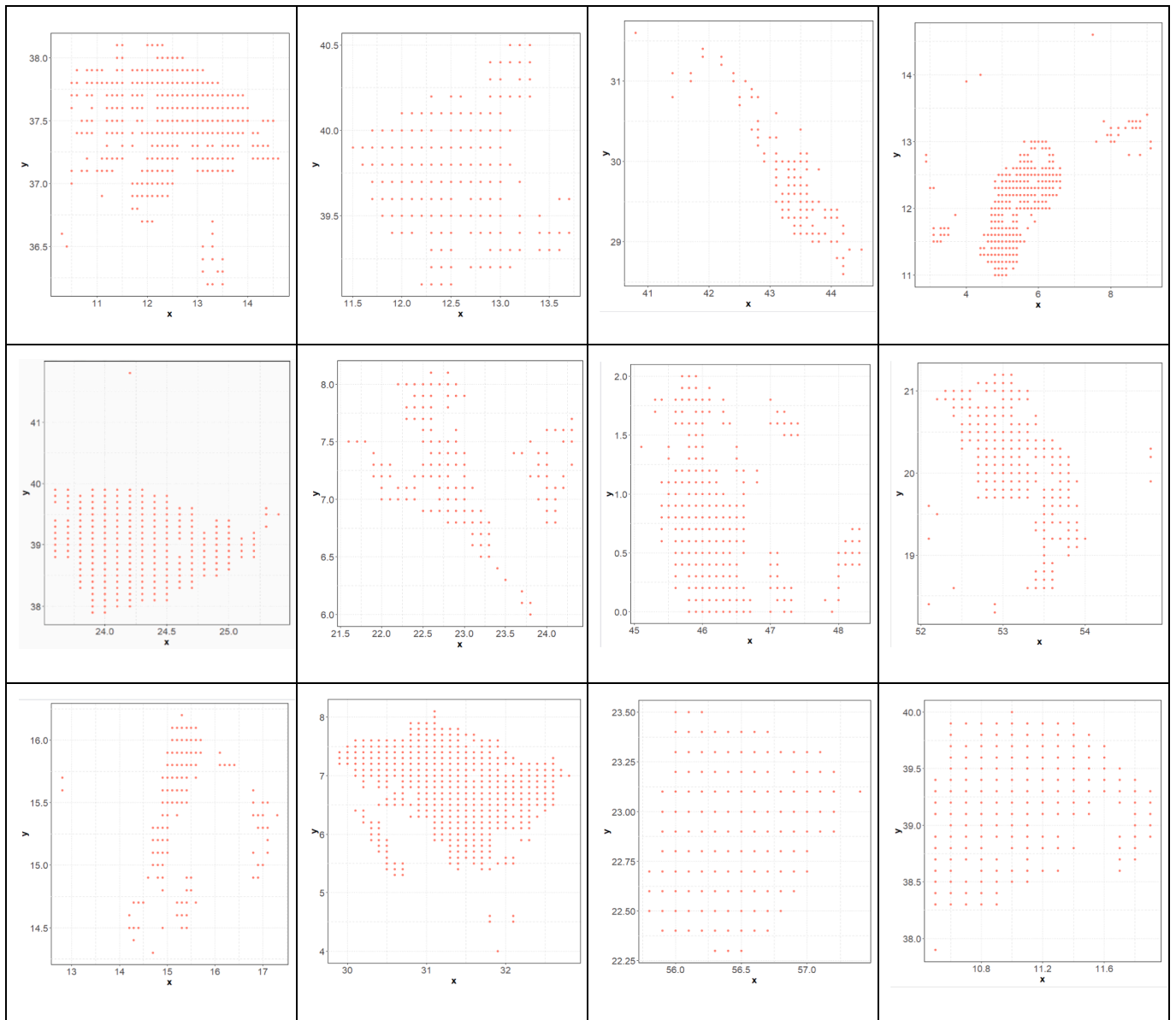
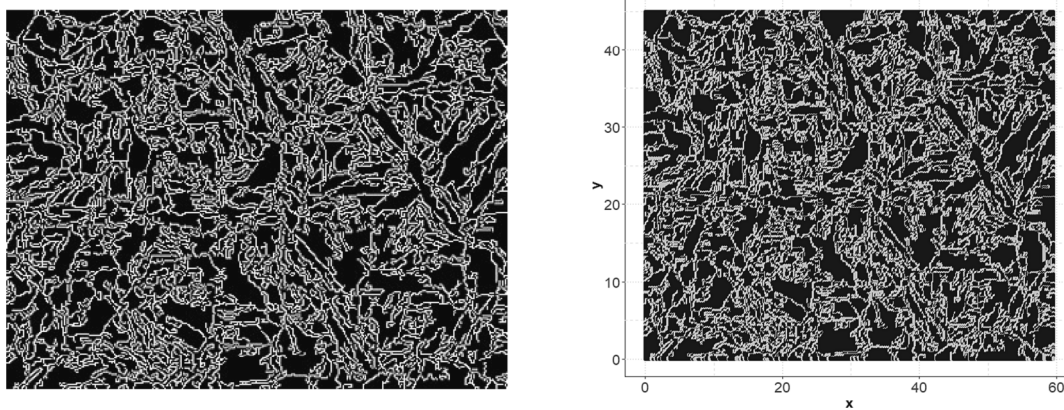**Fig. 4.** Representative grains detected by k-means++.

Fig. 5. Segmented grain boundaries; (left) Original image, (right) k-means++ clustered image.
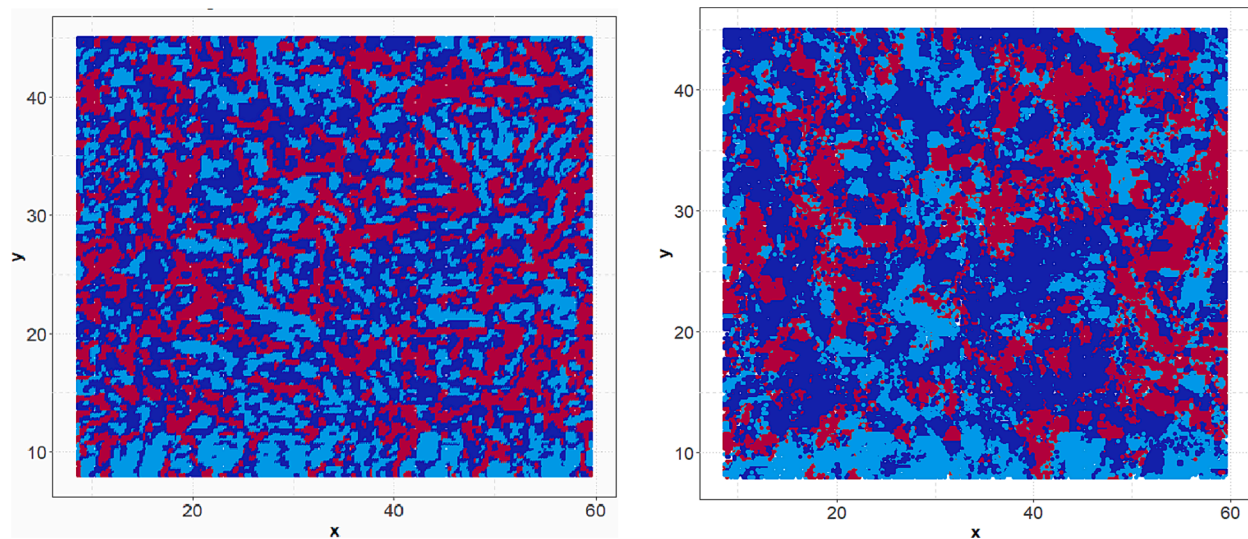
Fig. 6. EBSD generated phase map (left), and after reconstruction using image correlation with grain locations and the consensus algorithm P/M classification (right).
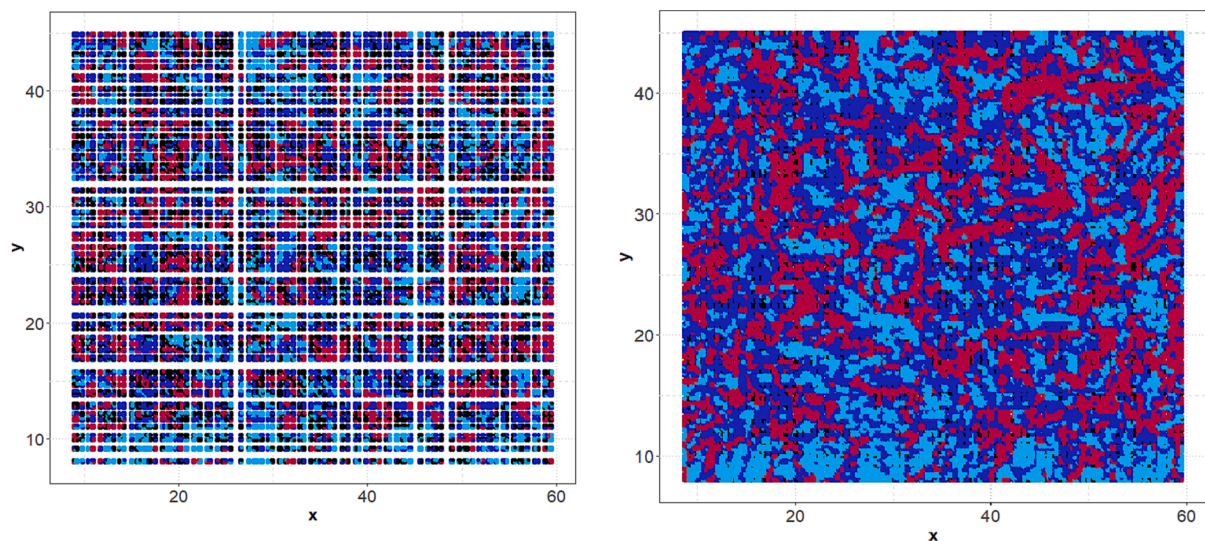

Fig. 7. Phases/microstructures and grain boundaries combined maps; (left) keeping the exact coordinates (x,y) in common between ebsd phase map and ipf map, (right) keeping the coordinates (x,y) in common within the ebsd phase map and ipf map and merging the rest of the x,y coordinates of ebsd phase map that were left out of the dataset during matching of the coordinates.

grains to detect the image edges. Thus, the initial IPF image was converted to the greyscale image shown below (Fig. 5, left) to recognize the grain boundaries by band contrast overlapping, the adopted method for this analysis. It is evident that the two-colored images properly show the position of the grains' edges. However, further processing with k-means color clustering (Fig. 5, right) was required to facilitate interpreting the image information. This was due to the original image containing thousands of color shades within the white, grey, and black spectrum.

3.4. Image clustering with k-means++ for grain merging

Fig. 6 (left) shows the phase distribution pixel-wise. Light blue represents the ferrite phase, deep blue indicates the bainite phase, and red corresponds to martensite. While similar methodologies for allocating pixels/scatters to specific phases are widely reported in literature, a common oversight is the assumption that each grain in the IPF map correlates to a single, distinct phase, which has not always been the case [38,39]. To address this, the next step involves using precise grain coordinates to establish a consensus algorithm. The algorithm will compare the distinct pixels within the grain boundaries against the population of colors (and, consequently, phase annotations). This process allows for determining the correct phase of each grain through consensus.

For this procedure, the phase map image from the EBSD analysis was clustered to reduce the number of color shades to only three. This reduction facilitates data interpretation and allows for a more accurate revision of the phases/microstructures (P/M) annotations within each grain, as indicated by IPF maps.

The next step in the analysis involved correlating the phase map image with the grain boundaries image. This was achieved by merging the two datasets and aligning the exact (x,y) coordinate pairs within each. However, this approach revealed that a significant amount of information was discarded due to mismatches in coordinates. This discrepancy often arises since it is not always possible to have the same coordinates when reading different image datasets (the IPF map and the generated EBSD phase map may have different coordinates in principle).
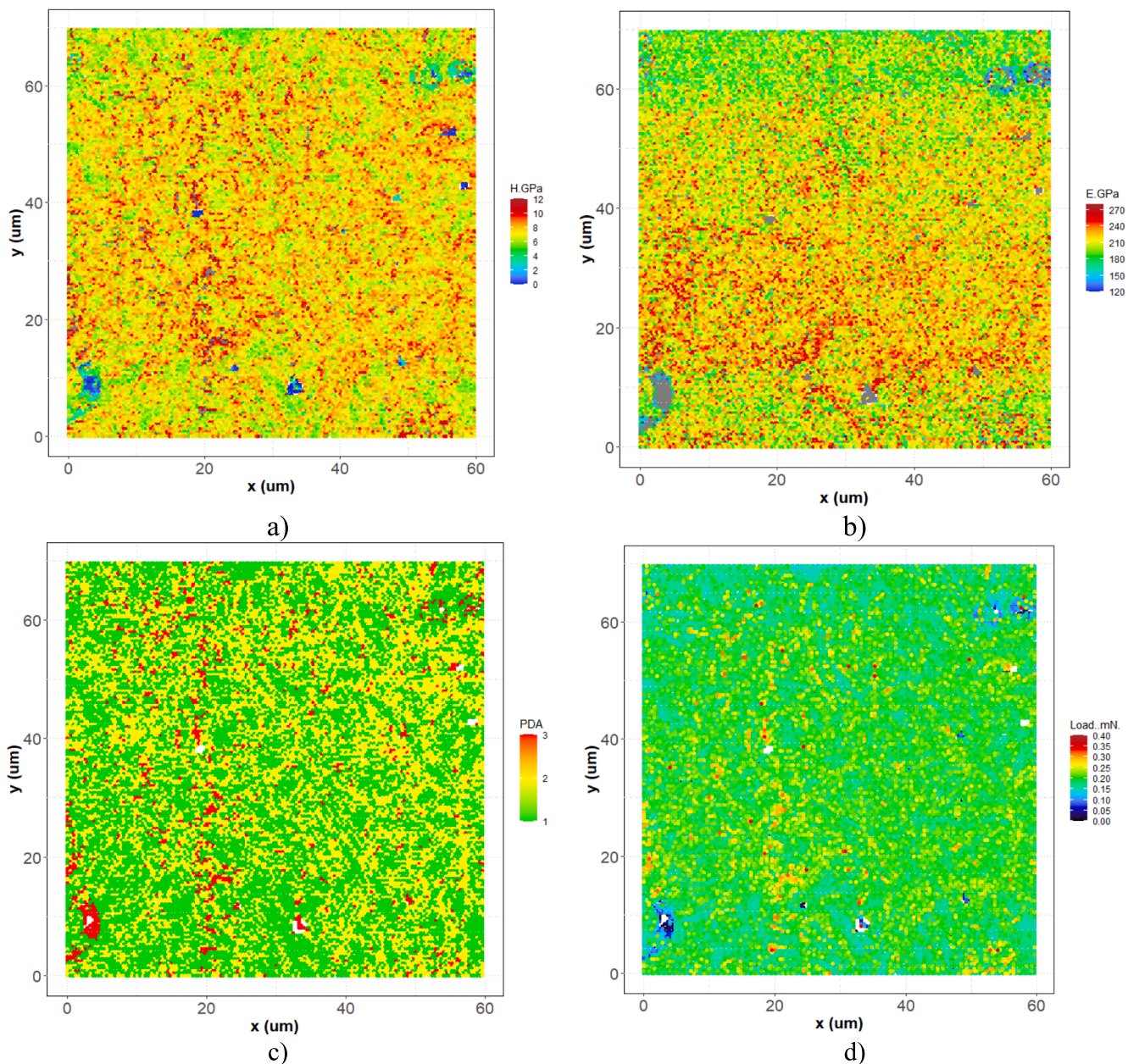
Fig. 8. Nanoindentation mapping: a) Hardness plot at 30 nm reporting depth; b) Indentation modulus at 30 nm reporting depth; c) Phase map using P, H, E_r data and Gaussian Mixture Models with Expectation Maximization algorithm to optimize the fitting, where phase 3 corresponds to martensite, 2 corresponds to bainite, and 1 corresponds to ferrite; d) Load distribution map.

For instance, a notable factor that can contribute to this issue is the electron image drift during EBSD measurement.

From the optical inspection of the combined maps in Fig. 7, it is evident that the problem of missing data could be addressed by merging the coordinates of EBSD phase map that do not match with the edges detected in the IPF map (right image). However, this approach contains inaccuracies, as boundaries might be just 100 nm away from matching the exact coordinates that would classify a datapoint as a grain boundary instead of a P/M. Another option is to incorporate a reduced dataset with exact coordinate matches across all techniques, specifically referring to nanoindentation data, which is the next step of the methodology. However, this step carries the risk of information loss.

3.5. Nanoindentation

Nanoindentation was performed in the same ROI (indicated by FIB

marks) as the EBSD mapping, immediately following the diffraction scanning. The nanoindentation maps, which illustrate the CSM of the TRIP within the range of 0–35 nm, report the nanomechanical properties at the 30 nm depth (Fig. 8). In total, over 25,000 data points were produced, providing statistical significance to the mechanical performance analysis of the investigated phases detected by nanoindentation. Below are the maps of indentation hardness, indentation modulus, and the distribution of applied load are presented.

To create the phase map, individual parameters were utilized to perform data clustering. This was achieved by applying the Gaussian Mixture Model (GMM) clustering to the displacement-controlled measurement data using the indentation modulus, hardness, and applied load as input parameters. This approach, illustrated in Fig. 8c helps to minize the bias due to the varying magnitudes of these descriptors. Three descriptors were adopted for cluster formation since it provides a more objective basis for classifying the formed phases than relying on a
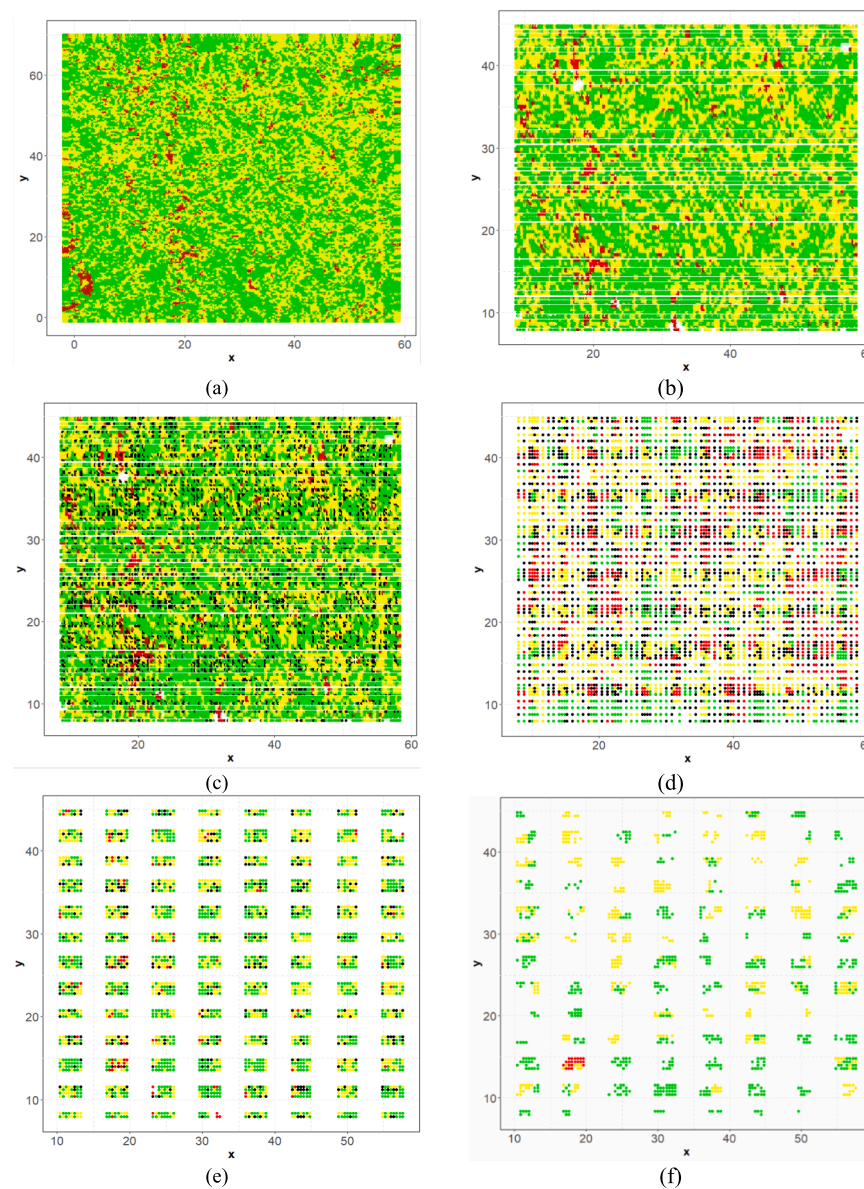
Fig. 9.. Correlation of nanoindentation and EBSD; (a) Clustered nanoindentation phase map utilizing the contour plot of GMM clustering with three parameters, (b) Merged map using nanoindentation map by overlapping EBSD data, (c) merging of refined nanoindentation map by consensus and EBSD IPF map; nanoindentation map with common coordinates with GBs, (d) merging of refined nanoindentation map and EBSD IPF map; nanoindentation scatter map with common coordinates with GBs and after revising the data of nanoindentation by EBSD phase annotation and grain consensus, (e) combined Nanoindentation and IPF scatter map refined by the actual nanoindentation measurement coordinates, and (f) revised nanoindentation scatter map by IPF and EBSD phase maps.

single parameter.

3.6. P/M validation through EBSD-calibrated nanoindentation

The nanomechanical phase map underwent preliminary treatment before correlation, being transformed in a contour plot to enhance the mapping with the knowledge of the grains coordinates. This plot was color clustered to reduce the color shades to three colors (Fig. 9a). The data treatment followed a similar consensus-based mechanism as used for the EBSD phase map, ensuring a more representative and realistic outcome.

Then, like the proposed methodology applied to EBSD image, the exact locations of the grain boundaries were correlated with the nanoindentation data. The nanoindentation data points that were left out in Fig. 9b were subsequently reintegrated in the dataframe, as shown in Fig. 9c. These data points were then cross-referenced with the structural phases of the EBSD map in Fig. 9d.

However, it should be emphasized that even though this methodology exploits the real data that are merged through ex-situ characterization at the exact same ROI, it introduces a significant level of information loss. To retain the added value of such correlations, it would be more favorable to devise a strategy that allows the utilization of this knowledge without losing approximately 90 % of the data during the subsequent merging procedures of the proposed methodology steps shown in Fig. 9e and Fig. 9f. This approach would also help in avoiding fuzzy processing of data.

By incorporating the phase map shown in Fig. 9e into the mapping data of grain boundaries, it becomes evident, as illustrated below, that a significant amount of data is missing. This issue becomes even more pronounced when performing phase correlation between nano-mechanical phases and structural phases of EBSD. In the final dataset, only about 10% of the total amount of the initial nanoindentation dataset population remains, corresponding to the 25,000 coordinates that indicate the location of nanoindentation. A similar pattern is
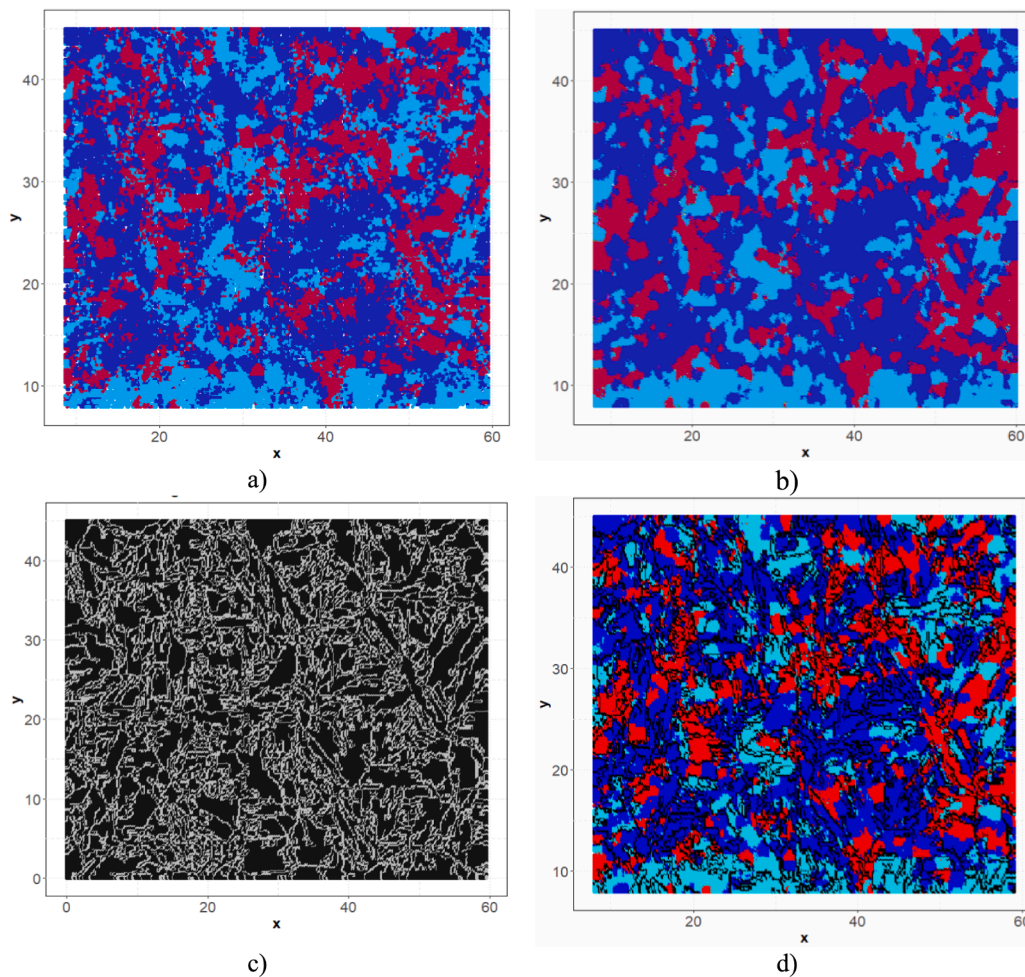
Fig. 10. A) original ebsd phase map with grain annotation, b) enhanced ebsd map by k-nn data imputation method, c) gbs data imputed map, d) enhanced combined dataset utilising the imputed data to generate the combined ebsd phase map with gbs.

observed when treating nanoindentation data alone and correlating it only with the grain boundaries. It should be noted, however, that higher image quality of EBSD maps could lead to larger datasets, thus reducing the number of missing points when correlating the exact (x,y) coordinate pairs.

3.7. Data imputation strategy to enhance characterization mapping correlation

An alternative pathway is presented below, which involves data imputation techniques to address the issue of missing data during characterization mapping correlations. Since the EBSD step size in the measurement was 0.1745 μm and the nanoindentation inter-indent spacing was 0.3 μm, data imputation was performed to provide interpolated data for every 0.1 μm in both x and y directions. The chosen "Artificial" data imputation method was applied to the EBSD phase map image, the IPF grain boundary image, and the nanoindentation phase map image datasets. This enabled training a k-NN (k-nearest neighbors) regression model for each case. Consequently, it became possible to predict the required values of the R, G, and B columns (i.e., their color) for the new dataset based on the corresponding eight nearest neighbors coordinates (x,y). In the end, the resulting colors were correlated with the structural phases, the grain boundaries, and the mechanical phases, respectively.

Below, the outcomes obtained by methodology above, enhanced by data imputations, are presented for both the IPF grain boundary map and the EBSD phase map. Firstly, Fig. 10b presents the EBSD phase map

which appears slightly smoother compared to the original map in Fig. 10a. This original map also includes information on the matching (x, y) pairs of the grain boundaries. Finally, Fig. 10c shows the enhanced grain boundaries map after clustering, used for data correlation with the EBSD phase map (Fig. 10d).

The same procedure was applied to the nanoindentation map image to extract (x, y) coordinates and color R, G, B values and to enhance the (x,y) information of the dataset by varying within the minimum and maximum coordinate values by 0.1 μm. It is noticeable that there are only a few differences between the original and the imputed image, indicating that data imputation also yielded reliable results in the case of the mechanical phase mapping (Fig. 10, Fig. 11). A similar observation is made after the subsequent clustering to reduce the number of color shades appearing to the image. Following this, the consensus algorithm was applied to annotate the phase map at grain specific level and make the mechanical map more representative of the actual surficial topology of the TRIP sample.

The following steps involved annotating the grain boundaries in the nanoindentation mechanical map to correctly identify the data points and properties related to the classified phases and grain boundaries. This process was essential for removing any bias affecting the statistical analysis. A similar analysis was carried out for phase analysis, but based on the EBSD structural phase annotation for comparison. All image datasets were used to obtain a subset with over 25,000 nanoindentation data points. This number was reduced to about 16,000 datapoints when focusing on the exact same boundary coordinates as those in the EBSD phase map. This reduction occurred because the final EBSD map
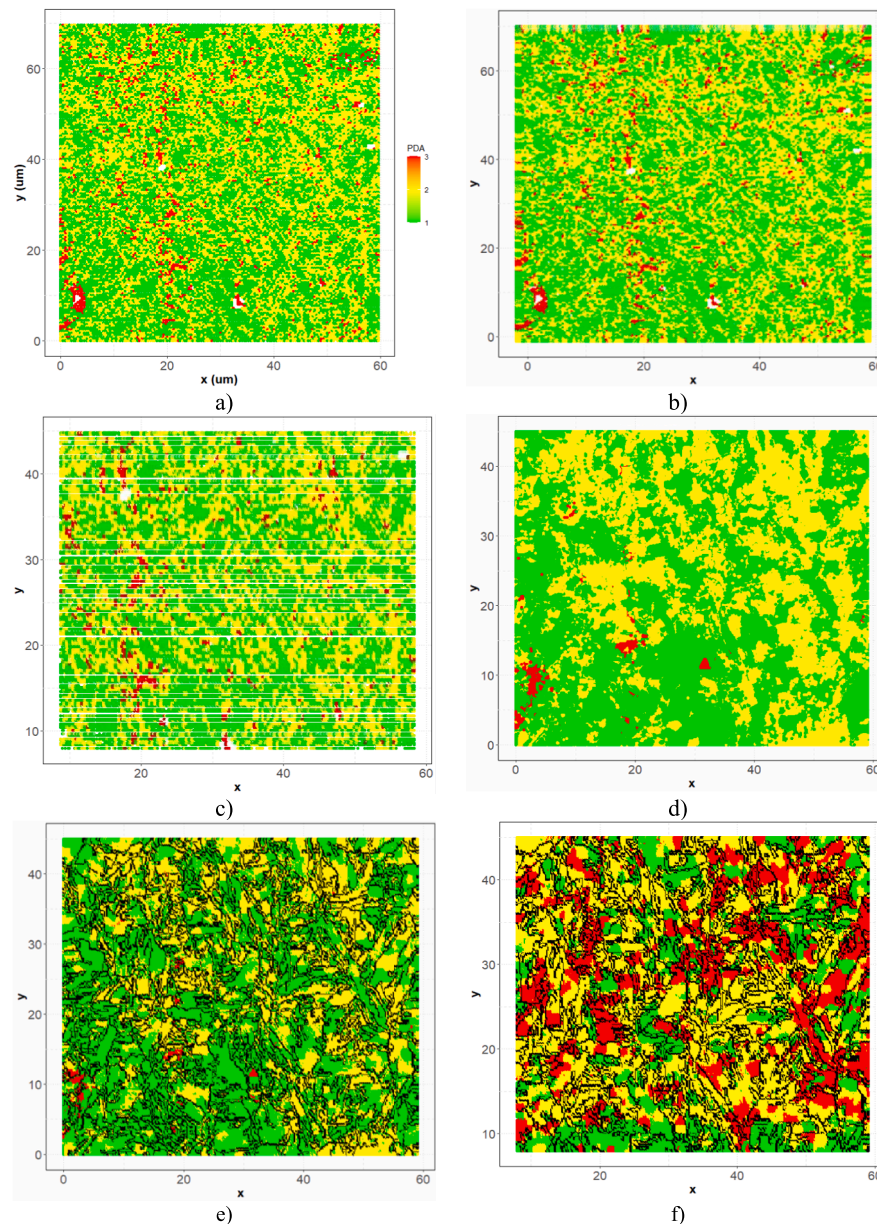
Fig. 11. Merging of P/M map and nanoindentation raster; a) original nanoindentation map, b) imputed nanoindentation map, c) refined original nanoindentation map considering the exact grain locations, d) refined imputed nanoindentation map considering the exact grain locations, e) original nanoindentation map with the introduction of grain boundaries, refined by EBSD phase map, f) imputed nanoindentation map with the introduction of grain boundaries, refined by EBSD phase map.

corresponded to a smaller Region of Interest (ROI) than the nano-indentation data.

3.8. Extraction of nanomechanical properties statistics for each P/M and crystallographic planes

Upon examining the subsequent treatment steps of the nano-mechanical phase map, it is evident that the clusters were initially formed based on the contrast/difference in nanomechanical properties. This methodology, using the Gaussian mixture model (GMM), was employed to associate groups of data with structural phases. However, the initial phase annotation, based on the nanomechanical properties and the GMM model, did not align with the scientific understanding (See Table 2-1). This can be explained by considering that each grain is characterized by one microstructure, and the response should be evaluated at this level. Notably, the martensite properties were initially

associated with the lowest modulus and highest hardness, which presents a contradiction.

As can be pointed out, with the application of the Gaussian Mixture Model, the cluster with higher hardness was attributed to martensite. In contrast, the softest cluster was associated with ferrite, as referenced in various studies [14,15,40,41]. However, it should be noted that this cluster also demonstrated the minimum mean value for elastic modulus, which contradicts expectations based on existing literature [14].

Comparing experimental data with findings in the literature, the following observations were made:

• Bainite: elastic modulus [42] and hardness [7,40,41] values are comparable to literature values. In fact, for hardness, literature values are close to 6.2–9 GPa[7,40,41]. However, some studies report lower values [15,33,43].

Table 2

Phase statistics of nanomechanical properties and grain size.

1) Nanoindentation map (contour) with annotation of phases by GMM clustering method.

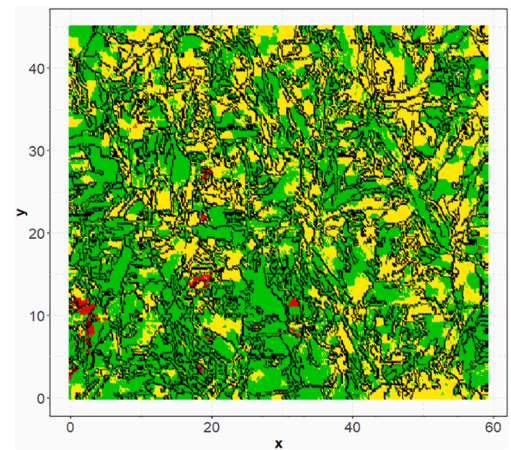| Phase	Mean E_r (GPa)	Standard deviation H (GPa)	Standard deviation E_r (GPa)	Mean H (GPa)
Bainite	214	0.91	20.0	8.03
Ferrite	213	0.88	23.1	6.61
Martensite	195	3.40	58.3	9.51
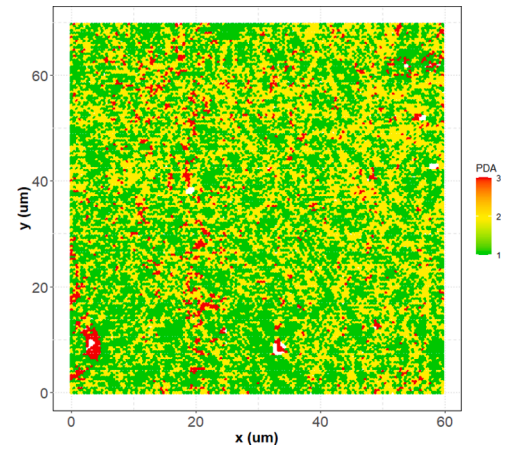
2) Nanoindentation map (contour) with grain correction and nanoindentation phase and coordinate refinement by consensus of the observations within the boundaries of each individual grain.

Phase	Mean E_r (GPa)	Standard deviation E_r (GPa)	Mean H (GPa)	Standard deviation H (GPa)
Bainite	218	21.7	7.85	1.32
Ferrite	217	24.9	7.29	1.32
Martensite	179	66.7	6.90	3.23
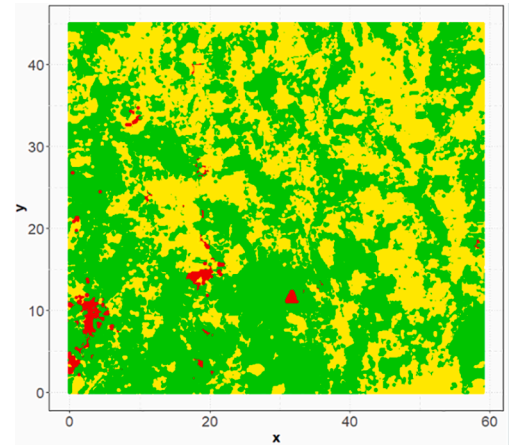
3) Nanoindentation map (contour) with grain correction and nanoindentation phase refinement by consensus of the observations within the boundaries of each individual grain and the annotation of the data belonging to GBs.

Phase	Mean E_r (GPa)	Standard deviation E_r (GPa)	Mean H (GPa)	Standard deviation H (GPa)
Bainite	218	21.7	7.84	1.87
Ferrite	217	25.0	7.29	1.88
GBs	218	24.5	7.55	2.01
Martensite	175	65.6	6.83	3.26

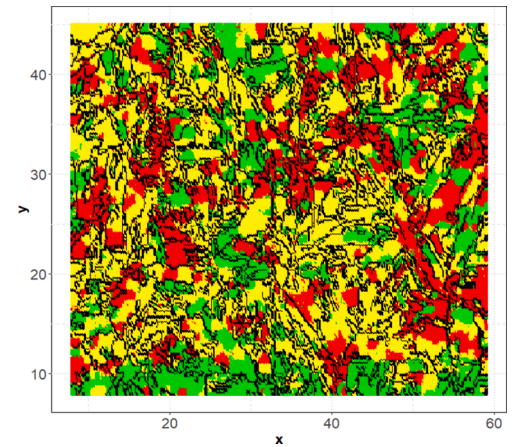4) Nanoindentation refined map (scatter plot) with annotation of phases by EBSD and GBs.

Phase	Mean E_r (GPa)	Standard deviation E_r (GPa)	Mean H (GPa)	Standard deviation H (GPa)

Table 2 (*continued*)

Phase				
Bainite	220	20.7	7.69	1.32
Ferrite	218	23.8	7.59	1.38
GBs	220	19.6	7.67	1.30
Martensite	219	21.5	7.64	1.31
Phase	Mean diameter (µm)	Standard deviation diameter (µm)	Mean length (µm)	Standard deviation length (µm)
Bainite	1.90	0.485	3.36	1.87
Ferrite	1.86	0.495	3.24	1.90
Martensite	1.86	0.470	3.17	1.76

5) Anisotropic plane statistics of nanoindentation map with annotation of phases by EBSD and addition of GBs.

Crystallographic plane	Mean E_r (GPa)	Standard deviation E_r (GPa)	Mean H (GPa)	Standard deviation H (GPa)
(001)	220	19.5	7.64	1.17
(001)U(101)	219	22.8	7.55	1.32
(001)U(111)	219	21.9	7.66	1.38
(101)	218	22.6	7.64	1.31
(101)U(111)	218	18.8	7.60	1.25
(111)	220	22.7	7.73	1.46
No plane	220	19.6	7.67	1.30
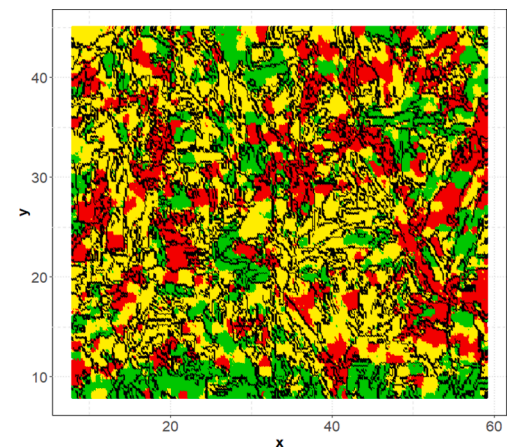
- Ferrite: elastic modulus values are close to those which can be found in the literature [13,14,40]. In addition, hardness values are similar to those reported by *Bassini E. et al.* [7], although lower values between 4.7–2 GPa [13–15,33,40,43] are also reported.
- Martensite: elastic modulus [14,33,44] and hardness [17,45,45] values are comparable with those reported in the literature [14,29,38 17,41,41]. Other reported lower values are inside the error bars [14,15].

The wide range of hardness and elastic modulus values in each grain can be attributed to multiple factors, such as carbon amount inside the grains, dislocations [40] and grain junctions within the same indent area [33]. Nevertheless, the fuzzy approaches and lack of validation for mechanical testing data used in phase annotation indicate the need for an object-oriented approach that minimizes subjective decisions. The present study may catalyze further developments in technology, promoting a more conscious integration of artificial intelligence. A deeper understanding of both materials science and data science principles is essential for this integration. Artificial Intelligence can pave the way for accelerating validation schemes and maximize the use of the vast amounts of data available, thus enhancing the construction of a comprehensive knowledge base for material relationships.

Upon revising the phases at grain-level, the results showed a negative correlation with martensite (See Table 2-2). This outcome might be connected to the effect of grain boundary indentations and composite mechanical responses observed when indentations are performed close to grain edges. A further step involved revising the nanomechanical properties by introducing a new class of grain boundary indentation regions. Despite these revisions, martensite still exhibited lower modulus and hardness values (See Table 2-3). However, when the nanomechanical properties were annotated with structural information obtained from diffraction, the nanomechanical properties of martensite aligned more closely with those of Bainite, Ferrite, and the nano-mechanical properties recorded at grain boundaries (See Table 2-4). These values were similar and fell within the standard deviation of the other phases. This result, validated by structural characterization, was the gold standard for assessing nanomechanical phase annotations.

Despite these efforts, the properties of martensite still do not show a clear distinction from other P/Ms properties in a data-driven way. Consequently, the EBSD phase annotation approach is considered more credible (See Table 2-5). This is because the structural phases and their properties are closer to the expected theoretical outcomes, with Martensite, Bainite and Ferrite having very similar properties. This similarity in properties can be attributed to the heat treatment, which affects the grain size and, consequently, their relative equivalent circular diameter. These values exhibit very close proximity among all phases. The table above presents the extracted properties at each stage of data exploitation.

Regarding grain statistics corresponding to the nanomechanical properties per crystallographic plane, it appears that the anisotropy of crystallographic planes does not significantly affect the nanomechanical response profile.

Regarding martensite, it has a body-centered tetragonal (BCT) lattice, which is produced by the Bain transformation of FCC lattices (austenite) [46]. To address this complexity, it was assumed, as a first approximation, that the crystallographic orientation of the BCT lattice is similar to that of BCC ones. This strategy is supported by literature [47]. In the case of bainite, it was assumed to be BCC, considering its ferritic
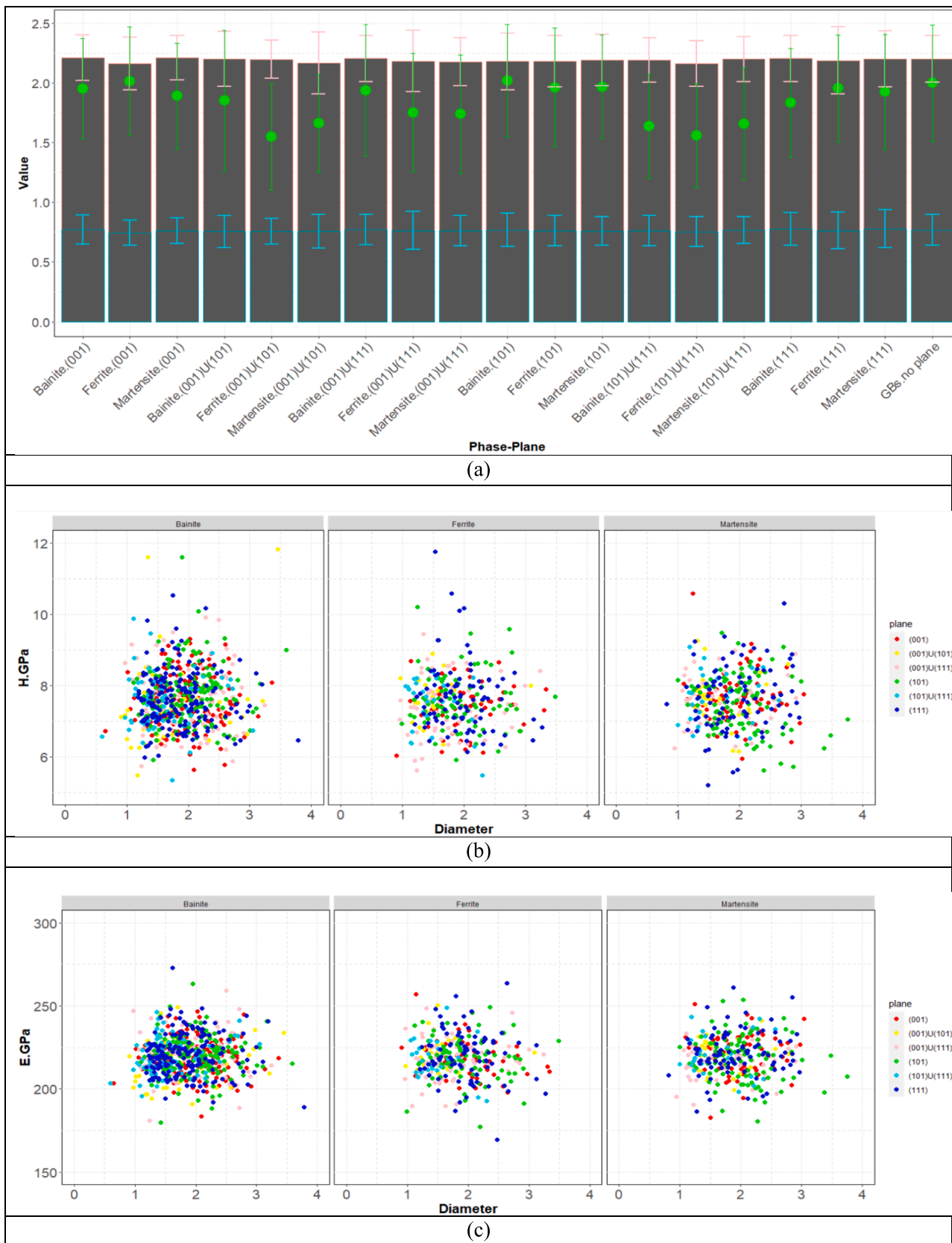
(a)

(b)

(c)

Fig. 12. (a) Plot of mean hardness (in blue), mean modulus (in orange), and the corresponding mean diameter (in green) for each phase and anisotropic plane for the final revised dataset by nanoindentation, grains, and EBSD phases. Hardness (in GPa/10) and modulus (in GPa/100) have been scaled for enhanced visualization. The diameter is presented in µm units. Plot of (b) hardness, and (c) indentation modulus vs the corresponding diameter of each grain for each phase detected. The colorscale corresponds to the anisotropic planes. The data presented correspond to the final revised dataset by nanoindentation, grains, and EBSD phases. Observations correspond to each identified grain. (For interpretation of the references to color in this figure legend, the reader is referred to the web version of this article.)

matrix.

Moreover, the mean indentation modulus and hardness were found to be independent of the crystals' orientation. Overall, it has been observed that the grain boundaries are associated with similar or higher hardness compared to the grain phases or planes [48]. The statistics derived from grain anisotropy indicate that anisotropy can affect the overall mechanical response. This observation implies that the initial mechanical phase mapping by nanoindentation may lead to contradictory conclusions when the microstructural, mechanical response is governed by anisotropy.

However, this does not seem to be the case in the specific class of steels being studied. The countertrend observed in elastic modulus values can be explained by a high percentage of "purely" ferritic grains (i.e., of polygonal origin). Therefore, the indented ferrite is often found within granular bainite, which comprises blocky retained austenite/martensite among irregular ferrite [40]. These features also affect the anisotropic properties, explaining the similar values of elastic modulus observed.

Finally, in Fig. 12b and Fig. 12c it can be observed that there is no correlation between grain size and mechanical properties, which could be since the indent area is smaller than the grain size. This behavior contrasts with micro- and macro-indentation, wherein multiple grains are intercepted in the indent area and the mechanical properties follow the Hall-Petch equation [49,50].

4. Conclusions

Our approach ensures each pixel group represents one phase and one grain with consistent boundaries, effectively avoiding contradictory classifications of data coordinates, such as a pixel classified as bainite adjacent to one classified as martensite, while both belong to the same grain. According to the consensus, each grain is represented by a single, specific phase.

Furthermore, this methodology allows for the resolution of some ambiguous procedures that have previously been used to correlate nanoindentation hardness or modulus maps with EBSD data. This proposed methodology is expected to significantly impact and apply to other multiphase steels with similar microstructures, specifically noting that the mechanical properties alone may not be sufficient to distinguish appropriately the structural phases. Also, in this study, the presented properties are isolated from the grain boundary responses (data are excluded when presenting individual phases' average properties). In contrast, the occurrence of the Hall-Petch phenomenon was studied, but not evidenced, which indicated that the presented properties were free of the effects of grain boundaries indentation in such large statistical sample corresponding to the investigated ROI. Furthermore, when the same characterization techniques are applied to dual phase steels, other classes of TRIP steels, or any other type of steel, the versatility of this approach becomes evident.

The modular approach reported in this study enables various data elaboration processes, such as classifying an EBSD map, correlating different characterization maps, augmenting the datasets to ensure one-to-one correlations without information loss with the synthetic data method, performing optimized clustering of color images/maps, and extracting patterns for materials P/M structure, properties, and size. Additionally, validating nanoindentation phase analysis data against EBSD phase maps, combined with data science techniques, can provide the capacity to establish and reuse a curated dataset. This approach can be extended by employing transfer learning with a trained machine learning to facilitate the analysis of TRIP with similar composition.

CRediT authorship contribution statement

Federico Bruno: Writing – original draft, Visualization, Methodology, Investigation, Formal analysis. **Georgios Konstantoupoulos:** Writing – original draft, Visualization, Validation, Supervision, Software, Methodology, Investigation, Formal analysis, Data curation, Conceptualization. **Gianluca Fiore:** Investigation. **Edoardo Rossi:** Writing – review & editing, Validation, Investigation, Formal analysis, Data curation, Conceptualization. **Marco Sebastiani:** Writing – review & editing, Validation, Supervision, Resources, Funding acquisition. **Costas Charitidis:** . **Luca Belforte:** Writing – review & editing, Supervision, Investigation. **Mauro Palumbo:** Writing – review & editing, Validation, Supervision, Resources.

Declaration of competing interest

The authors declare that they have no known competing financial interests or personal relationships that could have appeared to influence the work reported in this paper.

References

[1] Oxford Instruments, https://www.oxinst.com/blogs/correlative-microscopy-the-microscopists-dilemma, (2023).

[2] AHSS Application Guidelines - WorldAutoSteel, https://ahssinsights.org/metallurgy/steel-grades/3rdgen-ahss/transformation-induced-plasticity-trip/), (2023).

[3] W. Nicodemi, Acciai e Leghe Non Ferrose (2008).

[4] K. Kaufmann, C. Zhu, A.S. Rosengarten, D. Maryanovsky, H. Wang, K.S. Vecchio, K.S. Vecchio, Phase mapping in EBSD using convolutional neural networks, Microsc. Microanal. 26 (2020) 458–468, https://doi.org/10.1017/S1431927620001488.

[5] Oxford Instruments, https://www.ebsd.com/ois-ebsd-system/advanced-phase-discrimination, (2023).

[6] K. Kaufmann, H. Lane, X. Liu, K.S. Vecchio, Efficient few-shot machine learning for classification of EBSD patterns, Sci. Rep. 11 (2021), https://doi.org/10.1038/s41598-021-87557-5.

[7] E. Bassini, G. Marchese, A. Sivo, P.A. Martelli, A. Gullino, D. Ugues, Effect of cold rolling on microstructural and mechanical properties of a dual-phase steel for automotive field, Materials 15 (2022), https://doi.org/10.3390/ma15217482.

[8] M. Nowell, S. Wright, J. Carpenter, Differentiating Ferrite and Martensite in Steel Microstructures Using Electron Backscatter Diffraction, 2009. https://www.researchgate.net/publication/267777956.

[9] S. Zaefferer, P. Romano, F. Friedel, EBSD as a tool to identify and quantify bainite and ferrite in low-alloyed al-TRIP steels, J Microsc 230 (2008) 499–508, https://doi.org/10.1111/j.1365-2818.2008.02010.x.

[10] M.S. Baek, K.S. Kim, T.W. Park, J. Ham, K.A. Lee, Quantitative phase analysis of martensite-bainite steel using EBSD and its microstructure, tensile and high-cycle fatigue behaviors, Mater. Sci. Eng. A 785 (2020), https://doi.org/10.1016/j.msea.2020.139375.

[11] J.Y. Kang, S.J. Park, M.B. Moon, Phase analysis on dual-phase steel using band slope of electron backscatter diffraction pattern, Microsc. Microanal. 19 (2013) 13–16, https://doi.org/10.1017/S1431927613012233.

[12] G. Cheng, K.S. Choi, X. Hu, X. Sun, Application of Nano-indentation test in estimating constituent phase properties for microstructure-based modeling of multiphase steels, SAE Int J Engines 10 (2017) 405–412, https://doi.org/10.4271/2017-01-0372.

[13] S. Bhowmick, M.M. Nowell, Mechanical properties of ferrite and austenite phases in duplex steel, A Combined EBSD and SEM Nanoindentation Study (2016).

[14] T. Zhang, H. Xie, M. Huo, F. Jia, L. Li, D. Pan, H. Wu, J. Liu, T. Yang, F. Jiang, Z. Jiang, A method for the determination of individual phase properties in multiphase steels, Mater. Sci. Eng. A 854 (2022), https://doi.org/10.1016/j.msea.2022.143707.

[15] Y. Chang, M. Lin, U. Hangen, S. Richter, C. Haase, W. Bleck, Revealing the relation between microstructural heterogeneities and local mechanical properties of complex-phase steel by correlative electron microscopy and nanoindentation characterization, Mater Des 203 (2021), https://doi.org/10.1016/j.matdes.2021.109620.

[16] P. Burik, L. Pesek, P. Kejzlar, Z. Andrsova, P. Zubko, Effect of crystallographic orientations of grains on the global mechanical properties of steel sheets by depth

sensing indentation, J. Phys. Conf. Ser., Inst. Phys. Publ. (2017), https://doi.org/10.1088/1742-6596/790/1/012003.

[17] R. Lehnert, A. Weidner, M. Motylenko, H. Biermann, Strain hardening of phases in high-alloy CrMnNi steel as a consequence of pre-deformation studied by nanoindentation, Adv. Eng. Mater. 21 (2019), https://doi.org/10.1002/adem.201800801.

[18] R.A. Rijkenberg, M.P. Aarnts, F.A. Twisk, M.J. Zuijderwijk, M. Knieps, H. Pfaff, Linking crystallographic, chemical and nano-mechanical properties of phase constituents in DP and TRIP steels, Mater. Sci. Forum, Trans. Tech. Publ. Ltd. (2010) 3465–3472, https://doi.org/10.4028/www.scientific.net/MSF.638-642.3465.

[19] T.H. Ahn, C.S. Oh, D.H. Kim, K.H. Oh, H. Bei, E.P. George, H.N. Han, Investigation of strain-induced martensitic transformation in metastable austenite using nanoindentation, Scr Mater 63 (2010) 540–543, https://doi.org/10.1016/j.scriptamat.2010.05.024.

[20] I. Sapezanskaia, J.J. Roa, G. Fargas, M. Turon-Viñas, T. Trifonov, R. Kouitat Njiwa, A. Redjaïmia, A. Mateo, Deformation mechanisms induced by nanoindentation tests on a metastable austenitic stainless steel: a FIB/SIM investigation, Mater Charact 131 (2017) 253–260, https://doi.org/10.1016/j.matchar.2017.07.019.

[21] Y. Kim, T.H. Ahn, D.W. Suh, H.N. Han, Variant selection during mechanically induced martensitic transformation of metastable austenite by nanoindentation, Scr. Mater. 104 (2015) 13–16, https://doi.org/10.1016/j.scriptamat.2015.03.014.

[22] S. Janakiram, P.S. Phani, G. Ummethala, S.K. Malladi, J. Gautam, L.A.I. Kestens, New insights on recovery and early recrystallization of ferrite-pearlite banded cold rolled high strength steels by high speed nanoindentation mapping, Scr Mater 194 (2021), https://doi.org/10.1016/j.scriptamat.2020.113676.

[23] B. Vignesh, W.C. Oliver, G.S. Kumar, P.S. Phani, Critical assessment of high speed nanoindentation mapping technique and data deconvolution on thermal barrier coatings, Mater Des 181 (2019), https://doi.org/10.1016/j.matdes.2019.108084.

[24] E. Rossi, J.M. Wheeler, M. Sebastiani, High-speed nanoindentation mapping: A review of recent advances and applications, Current Opinion in Solid State and Materials Science 27 (5) (2023) 101107, https://doi.org/10.1016/j.cossms.2023.101107.

[25] G. Konstantopoulos, E.P. Koumoulos, C.A. Charitidis, Digital innovation enabled nanomaterial manufacturing; machine learning strategies and green perspectives, Nanomaterials 12 (2022), https://doi.org/10.3390/nano12152646.

[26] E. Koumoulos, G. Konstantopoulos, C. Charitidis, Applying machine learning to nanoindentation data of (nano-) enhanced composites, Fibers 8 (2020), https://doi.org/10.3390/fib8010003.

[27] M. Frelek-Kozak, L. Kurpaska, M. Lesniak, I. Jozwik, J. Jagielski, Mechanical and structural properties of ODS RAF steels submitted to low-energy ions irradiation, Fusion Eng. Des. 127 (2018) 54–59, https://doi.org/10.1016/j.fusengdes.2017.12.006.

[28] L. Kurpaska, Nanomechanical investigation of ion implanted single crystals – challenges, possibilities and pitfall traps related to nanoindentation, Nucl Instrum Methods Phys Res B 409 (2017) 171–174, https://doi.org/10.1016/j.nimb.2017.04.052.

[29] Z. Wang, H. Bei, E.P. George, G.M. Pharr, Influences of surface preparation on nanoindentation pop-in in single-crystal mo, Scr Mater 65 (2011) 469–472, https://doi.org/10.1016/j.scriptamat.2011.05.030.

[30] A. Ruiz-moreno, P. Hähner, L. Kurpaska, J. Jagielski, P. Spätig, M. Trebala, S. P. Hannula, S. Merino, G. de Diego, H. Namburi, O. Libera, D. Terentyev, T. Khvan, C. Heintze, N. Jennett, Round robin into best practices for the determination of indentation size effects, Nanomaterials 10 (2020), https://doi.org/10.3390/nano10010130.

[31] A. Dhal, R. Sankar Haridas, P. Agrawal, S. Gupta, R.S. Mishra, Mapping hierarchical and heterogeneous micromechanics of a transformative high entropy alloy by nanoindentation and machine learning augmented clustering, Mater Des 230 (2023), https://doi.org/10.1016/j.matdes.2023.111957.

[32] M.J. Uddin, E. Ramirez-Cedillo, R.A. Mirshams, H.R. Siller, Nanoindentation and electron backscatter diffraction mapping in laser powder bed fusion of stainless steel 316L, Mater Charact 174 (2021), https://doi.org/10.1016/j.matchar.2021.111047.

[33] R.M. Jentner, K. Srivastava, S. Scholl, F.J. Gallardo-Basile, J.P. Best, C. Kirchlechner, G. Dehm, Unsupervised clustering of nanoindentation data for microstructural reconstruction: challenges in phase discrimination, Materialia (oxf) 28 (2023), https://doi.org/10.1016/j.mtla.2023.101750.

[34] C.M. Magazzeni, H.M. Gardner, I. Howe, P. Gopon, J.C. Waite, D. Rugg, D.E. J. Armstrong, A.J. Wilkinson, Nanoindentation in multi-modal map combinations: a correlative approach to local mechanical property assessment, J Mater Res 36 (2021) 2235–2250, https://doi.org/10.1557/s43578-020-00035-y.

[35] ASTM, www.astm.org/e0415-21.html, (2021).

[36] Oxford Instruments, https://www.ebsd.com/hints-and-tips/ebsd-sample-preparation, (2023).

[37] W.C. Oliver, G.M. Pharr, An improved technique for determining hardness and elastic modulus using load and displacement sensing indentation experiments, Journal of Materials Research 7 (6) (1992) 1564–1583, https://doi.org/10.1557/jmr.1992.1564.

[38] R. Marin, H. Combeau, J. Zollinger, M. Dehmas, B. Rouat, A. Lamontagne, N. Loukachenko, L. Lhenry-Robert, σ-Phase formation in super austenitic stainless steel during directional solidification and subsequent phase transformations, Metall Mater Trans A Phys Metall Mater Sci 51 (2020) 3526–3534, https://doi.org/10.1007/s11661-020-05794-1.

[39] W.C. Lenthe, L. Germain, M.R. Chini, N. Gey, M. De Graef, Spherical indexing of overlap EBSD patterns for orientation-related phases – application to titanium, Acta Mater 188 (2020) 579–590, https://doi.org/10.1016/j.actamat.2020.02.025.

[40] Z. Xiong, A.A. Saleh, G. Casillas, S. Cui, E.V. Pereloma, Phase-specific properties in a low-alloyed TRIP steel investigated using correlative nanoindentation measurements and electron microscopy, J Mater Sci 55 (2020) 2578–2587, https://doi.org/10.1007/s10853-019-04077-4.

[41] Q. Furnémont, M. Kempf, P.J. Jacques, M. Gö Ken, F. Delannay, On the measurement of the nanohardness of the constitutive phases of TRIP-assisted multiphase steels, Mater. Sci. Eng. 328 (2002) 26–32, https://doi.org/10.1016/S0921-5093(01)01689-6.

[42] J. Chakraborty, P.P. Chattopadhyay, D. Bhattacharjee, I. Manna, Microstructural refinement of bainite and martensite for enhanced strength and toughness in high-carbon low-alloy steel, Metall Mater Trans A Phys Metall Mater Sci 41 (2010) 2871–2879, https://doi.org/10.1007/s11661-010-0288-1.

[43] Y. Chang, C. Haase, D. Szeliga, L. Madej, U. Hangen, M. Pietrzyk, W. Bleck, Compositional heterogeneity in multiphase steels: characterization and influence on local properties, Mater. Sci. Eng. A 827 (2021), https://doi.org/10.1016/j.msea.2021.142078.

[44] F. Lani, Q. Furnémont, T. Van Rompaey, F. Delannay, P.J. Jacques, T. Pardoen, Multiscale mechanics of TRIP-assisted multiphase steels: II, Micromechanical Modelling, Acta Mater 55 (2007) 3695–3705, https://doi.org/10.1016/j.actamat.2007.02.015.

[45] M.C. Taboada, M.R. Elizalde, D. Jorge-Badiola, Austempering in low-C steels: microstructure development and nanohardness characterization, J Mater Sci 54 (2019) 5044–5060, https://doi.org/10.1007/s10853-018-3159-6.

[46] Y. Gao, Y. Wang, Hidden pathway during fcc to bcc/bct transformations: crystallographic origin of slip martensite in steels, Phys Rev Mater 2 (2018), https://doi.org/10.1103/PhysRevMaterials.2.093611.

[47] M.A. Rehan, M. Thuvander, B. Högman, P.E. Skogholm, EBSD analysis of blocky structures in hardened and tempered microstructures of a 5 wt.% cr cold work tool steel, Metall. Microstruct. Anal. 10 (2021) 862–875, https://doi.org/10.1007/s13632-021-00805-y.

[48] L. Chamma, J.M. Pipard, A. Arlazarov, T. Richeton, J.S. Lecomte, S. Berbenni, A combined EBSD/NANOINDENTATION study of dislocation density gradients near grain boundaries in a ferritic steel, Materiaux Et Techniques 110 (2022), https://doi.org/10.1051/mattech/2022005.

[49] S.H. Whang, Introduction, Nanostructured Metals and Alloys, in, 2011.

[50] K. Karimi, H. Salmenjoki, K. Mulewska, L. Kurpaska, A. Kosińska, M.J. Alava, S. Papanikolaou, Prediction of steel nanohardness by using graph neural networks on surface polycrystallinity maps, Scr Mater 234 (2023), https://doi.org/10.1016/j.scriptamat.2023.115559.